PROCEEDINGS A

royalsocietypublishing.org/journal/rspa

Research

Cite this article: Downing CA, Zueco D. 2021 Non-reciprocal population dynamics in a quantum trimer. *Proc. R. Soc. A* **477**: 20210507. https://doi.org/10.1098/rspa.2021.0507

Received: 22 June 2021
Accepted: 20 October 2021

Subject Areas:
optics, solid-state physics, quantum physics

Keywords:
chirality, non-reciprocity, two-level systems, open quantum systems

Author for correspondence:
C. A. Downing
e-mail: c.a.downing@exeter.ac.uk

Electronic supplementary material is available online at https://doi.org/10.6084/m9.figshare.c.5705312.

THE ROYAL SOCIETY PUBLISHING

Non-reciprocal population dynamics in a quantum trimer

C. A. Downing[1] and D. Zueco[2]

[1]Department of Physics and Astronomy, University of Exeter, Exeter EX4 4QL, UK
[2]Instituto de Nanociencia y Materiales de Aragón (INMA), CSIC-Universidad de Zaragoza, Zaragoza 50009, Spain

CAD, 0000-0002-0058-9746; DZ, 0000-0003-4478-1948

We study a quantum trimer of coupled two-level systems beyond the single-excitation sector, where the coherent coupling constants are ornamented by a complex phase. Accounting for losses and gain in an open quantum systems approach, we show how the mean populations of the states in the system crucially depend on the accumulated phase in the trimer. Namely, for non-trivial accumulated phases, the population dynamics and the steady states display remarkable non-reciprocal behaviour in both the singly and doubly excited manifolds. Furthermore, while the directionality of the resultant chiral current is primarily determined by the accumulated phase in the loop, the sign of the flow may also change depending on the coupling strength and the amount of gain in the system. This directionality paves the way for experimental studies of chiral currents at the nanoscale, where the phases of the complex hopping parameters are modulated by magnetic or synthetic magnetic fields.

1. Introduction

Reciprocity in the animal kingdom is manifested by the evolution of reciprocal altruism: 'you scratch my back, and I will scratch yours' [1]. Aside from mere grooming, the consequences of reciprocity for the sharing of food, medicine and knowledge are profound. However, the breakdown of reciprocity, perhaps fuelled by a lack of affinity or obligation, can also lead to certain benefits for the non-reciprocator, who can profit from the non-reciprocal interaction [2].

In condensed matter physics, there is currently a revolution in the fabrication and mastery of nanostructures which can exploit quantum mechanics [3,4]. This progress promises a new paradigm of quantum technologies which seek to transform the modern world [5,6]. In particular, the field of quantum optics provides the ideal framework to describe light–matter interactions and the quantum aspects of the latest metamaterials, which are commonly built from nanoscopic lattices of meta-atoms [7–10]. Recently, it was noticed that the introduction of the concept of non-reciprocity into nanophotonic systems will have sweeping implications for the control of light–matter coupling [11–14], and hence for future quantum technology. Non-reciprocal interactions between meta-atoms in metamaterials can immediately be seen to be advantageous for future chiral devices, such as circulators and isolators, which rely on the directional transfer of energy and information at the nanoscale [15–22].

In 2017, Roushan *et al*. [23] reported the directional circulation of photons in a triangular loop of superconducting qubits. In a pioneering experiment for chiral quantum optics, the team observed chiral ground-state currents and probed the unusual quantum phases of strongly interacting photons (for a review of strongly interacting photons, see [24]). The required synthetic magnetic fields were realized by sinusoidally modulating their qubit–qubit couplings, which led to the necessary complex phases attached to the coherent coupling constants [25]. Such complex phases can appear in various ways; for example: in a real magnetic field through the Peierls substitution [26,27], via a Peierls tunnelling phase even in the absence of an external magnetic field [28], using a time-dependent coupling Hamiltonian [29,30], constructing synthetic gauge fields using synthetic lattices [31], using light-induced gauge potentials [32–34], designing inductor–capacitor circuits [35], by considering circularly polarized dipoles [36] or by careful pumping, which gives rise to complex potentials [37].

Inspired by the landmark experiment of Roushan *et al.* [23], who modelled their photonic system as harmonic oscillators, in this work we study a trimer of two-level systems (2LSs) in order to probe the whole energy ladder, including the effects of saturation due to the strong interactions. The 2LS approximation may be realized in an abundance of physical systems, as catalogued in [38], including superconducting qubits [39,40], cold atoms [41] and plasmons in metallic nanoparticles [42]. We consider our 2LS trimer in a triangular geometry (figure 1*a*), in order to form a loop which may enclose a non-trivial accumulated phase (depending on the phases of the complex hopping parameters), which is akin to an Aharonov–Bohm ring [43]. Importantly, we go beyond the single-excitation limit, which allows us to study the circulation of multiple excitations in our system as we modulate the amount of gain and loss in the trimer. Prior studies of trimers have primarily focused on including losses in a non-Hermitian Hamiltonian approach [44–52] (for a review of non-Hermitian classical and quantum physics, see [53]; for a review of non-Hermitian systems and topology, see [54]), while other investigations have employed an open quantum systems approach [55–57]. Here we employ a quantum master equation so that the dynamics is both stable and regular by construction, and in doing so we go beyond models restricted to strictly obeying non-Hermitian or $\mathcal{PT}$ symmetric Hamiltonians [58,59].

The rest of this work is organized as follows: in §2, we introduce our model; we reveal chiral steady states in §3; we present instances of non-reciprocal dynamics in §4; and in §5 we draw some conclusions. In addition, the electronic supplementary material provides some calculational details and figures.

2. Model

We consider a trimer of 2LSs, which interact via coherent qubit–qubit coupling. Importantly, we allow for the coupling constants to have non-zero complex phases, which is the key ingredient that allows non-reciprocity to emerge [60–64]. Effectively, we study the Aharonov–Bohm effect [43] in a tight-binding quantum ring with three sites, in an open quantum systems approach. The generated phase ϕ is both gauge invariant (the energies and eigenstates become dependent on the phase) and physically consequential (non-reciprocity is induced in the quantum transport). In

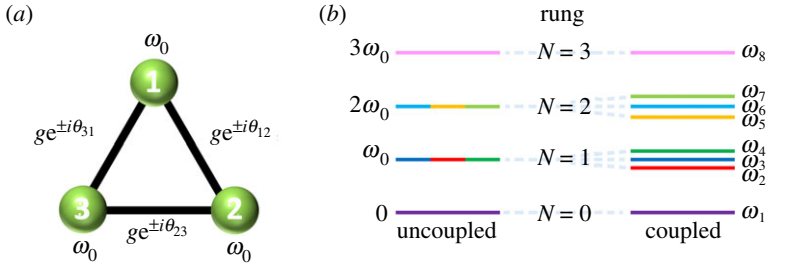

Figure 1. (*a*) A sketch of the trimer system, where each 2LS is of resonance frequency ω_0, and the magnitude of the three coupling constants is g. Each hopping is associated with a phase θ_{nn+1}. (*b*) The four-rung energy ladder of the trimer, codified by the number of excitations N, when the system is in the uncoupled (left) and coupled (right) regimes. (Online version in colour.)

§2a, where we introduce the Hamiltonian formulation, we show how the phase ϕ generalizes the eigenfrequencies. We include dissipation in the system in §2b, where we introduce the quantum master equation and incoherent gain processes.

(a) Hamiltonian

The Hamiltonian operator $\hat{H}$ for the system reads (we take $\hbar = 1$ throughout)

$$\hat{H} = \omega_0(\sigma_1^\dagger\sigma_1 + \sigma_2^\dagger\sigma_2 + \sigma_3^\dagger\sigma_3) + g(e^{i\theta_{12}}\sigma_1^\dagger\sigma_2 + e^{i\theta_{23}}\sigma_2^\dagger\sigma_3 + e^{i\theta_{31}}\sigma_3^\dagger\sigma_1 + \text{h.c.}), \tag{2.1}$$

where we have used cyclic boundary conditions, corresponding to the triangle geometry sketched in figure 1*a*. The transition frequency of each 2LS is ω_0 and the coherent coupling between 2LS-n and 2LS-$(n+1)$ is of magnitude $g \geq 0$ and phase θ_{nn+1}. The raising (lowering) operator of the nth 2LS is $\sigma_n^\dagger$ (σ_n), which satisfy the algebra of two distinguishable systems, with the anticommutator relation $\{\sigma_n, \sigma_n^\dagger\} = 1$ and the commutator relations $[\sigma_n, \sigma_m^\dagger] = [\sigma_n, \sigma_m] = 0$, where $n \neq m$. The Hamiltonian $\hat{H}$ of equation (2.1) defines four subspaces, spanned by the eigenstates corresponding to $N = \{0, 1, 2, 3\}$ excitations. Explicitly, the subspaces are given by

$$\{|\mathbf{0}\rangle\}, \quad N = 0, \tag{2.2a}$$

$$\{\sigma_1^\dagger|\mathbf{0}\rangle, \quad \sigma_2^\dagger|\mathbf{0}\rangle, \quad \sigma_3^\dagger|\mathbf{0}\rangle\}, \quad N = 1, \tag{2.2b}$$

$$\{\sigma_2^\dagger\sigma_1^\dagger|\mathbf{0}\rangle, \quad \sigma_3^\dagger\sigma_1^\dagger|\mathbf{0}\rangle, \quad \sigma_3^\dagger\sigma_2^\dagger|\mathbf{0}\rangle\}, \quad N = 2 \tag{2.2c}$$

and

$$\{\sigma_3^\dagger\sigma_2^\dagger\sigma_1^\dagger|\mathbf{0}\rangle\}, \quad N = 3, \tag{2.2d}$$

where the vacuum state, without any excitations, is $|\mathbf{0}\rangle = |0, 0, 0\rangle$. The energy ladder defined by equation (2.2) is sketched in figure 1*b*, in the weak (left) and strong (right) coupling regimes. The ground state is defined by $\hat{H}|\mathbf{0}\rangle = \omega_1|\mathbf{0}\rangle$, and has the eigenvalue $\omega_1 = 0$ (purple lines in figure 1*b*). The triply excited state is characterized by $\hat{H}\sigma_3^\dagger\sigma_2^\dagger\sigma_1^\dagger|\mathbf{0}\rangle = \omega_8\sigma_3^\dagger\sigma_2^\dagger\sigma_1^\dagger|\mathbf{0}\rangle$, and is associated with the maximal eigenvalue $\omega_8 = 3\omega_0$ (pink lines). These two extreme rungs of the energy ladder are the same in the coupled and uncoupled regimes (left and right in figure 1*b*), because they are associated with the wholly unoccupied state and the wholly occupied state. However, for the intermediate rungs associated with $N = \{1, 2\}$ excitations the nature of the coherent coupling is important. In the basis $\{\sigma_1^\dagger|\mathbf{0}\rangle, \sigma_2^\dagger|\mathbf{0}\rangle, \sigma_3^\dagger|\mathbf{0}\rangle\}$, the singly excited ($N = 1$) subspace has the 3×3 matrix representation

$$H_1 = \begin{pmatrix} \omega_0 & ge^{i\theta_{12}} & ge^{-i\theta_{31}} \\ ge^{-i\theta_{12}} & \omega_0 & ge^{i\theta_{23}} \\ ge^{i\theta_{31}} & ge^{-i\theta_{23}} & \omega_0 \end{pmatrix}, \tag{2.3}$$

royalsocietypublishing.org/journal/rspa Proc. R. Soc. A 477: 20210507

and the eigenvalues readily follow from equation (2.3) as

$$\omega_2 = \omega_0 + 2g\cos\left(\frac{\phi + 2\pi}{3}\right), \tag{2.4a}$$

$$\omega_3 = \omega_0 + 2g\cos\left(\frac{\phi + 4\pi}{3}\right) \tag{2.4b}$$

and

$$\omega_4 = \omega_0 + 2g\cos\left(\frac{\phi}{3}\right), \tag{2.4c}$$

where we have introduced the quantity

$$\phi = \theta_{12} + \theta_{23} + \theta_{31}, \tag{2.5}$$

which describes the accumulated phase ϕ in the trimer and is tantamount to the Aharonov–Bohm phase of a quantum ring [43]. Clearly, equation (2.4) exposes the first ramification of including non-trivial phases, even at the bedrock level of the eigenfrequencies, where it precipitates degeneracies at the trivial phases $\phi = \{0, \pi, 2\pi\}$ and otherwise presents non-trivial splittings of the energy levels. In the basis $\{\sigma_2^\dagger\sigma_1^\dagger|\mathbf{0}\rangle, \sigma_3^\dagger\sigma_1^\dagger|\mathbf{0}\rangle, \sigma_3^\dagger\sigma_2^\dagger|\mathbf{0}\rangle\}$, the doubly excited ($N = 2$) subspace has the 3×3 matrix representation

$$H_2 = \begin{pmatrix} 2\omega_0 & g\mathrm{e}^{-\mathrm{i}\theta_{12}} & g\mathrm{e}^{\mathrm{i}\theta_{31}} \\ g\mathrm{e}^{\mathrm{i}\theta_{12}} & 2\omega_0 & g\mathrm{e}^{-\mathrm{i}\theta_{23}} \\ g\mathrm{e}^{-\mathrm{i}\theta_{31}} & g\mathrm{e}^{\mathrm{i}\theta_{23}} & 2\omega_0 \end{pmatrix}, \tag{2.6}$$

such that the three eigenvalues of equation (2.6) are given by

$$\omega_5 = 2\omega_0 + 2g\cos\left(\frac{\phi + 2\pi}{3}\right), \tag{2.7a}$$

$$\omega_6 = 2\omega_0 + 2g\cos\left(\frac{\phi + 4\pi}{3}\right) \tag{2.7b}$$

and

$$\omega_7 = 2\omega_0 + 2g\cos\left(\frac{\phi}{3}\right), \tag{2.7c}$$

which are identical to equation (2.4) up to a constant shift in frequency of ω_0. We plot in figure 2 the eigenfrequencies ω_n of the energy ladder using equations (2.4) and (2.7), as a function of the accumulated phase ϕ (see equation (2.5)). Most notably, the accumulated phase ϕ crucially determines the magnitude, ordering and degeneracy of both the single-excitation subspace (red, blue and green lines) and double-excitation subspace (orange, cyan and lime lines) eigenfrequencies, in a manifestation of the Aharonov–Bohm effect [43] for a three-site quantum ring, going beyond the single-excitation sector.

Notably, a triangular trimer is the most elementary system in which the phase of the coherent coupling is important at the simplest-level of the eigenfrequencies. In a two-site dimer, with Hamiltonian $\hat{H}_{\mathrm{di}} = \omega_0(\sigma_1^\dagger\sigma_1 + \sigma_2^\dagger\sigma_2) + g(\mathrm{e}^{\mathrm{i}\theta_{12}}\sigma_1^\dagger\sigma_2 + \mathrm{h.c.})$, the single-excitation eigenfrequencies are unaffected by the phase θ_{12}. They simply read $\omega_\pm = \omega_0 \pm g$, such that the energy ladder of the dimer is formed by $\{2\omega_0, \omega_+, \omega_-, 0\}$ [36,65]. Moreover, a linear trimer (or indeed a linear chain of any size) will not support a gauge-independent phase, since it is crucial to have a ring geometry in order to mimic Aharonov–Bohm-style physics.

(b) Quantum master equation

Upon assuming weak coupling to the environment and Markovian behaviour, and after discarding fast-oscillating (non-resonant) terms, the quantum master equation of the trimer

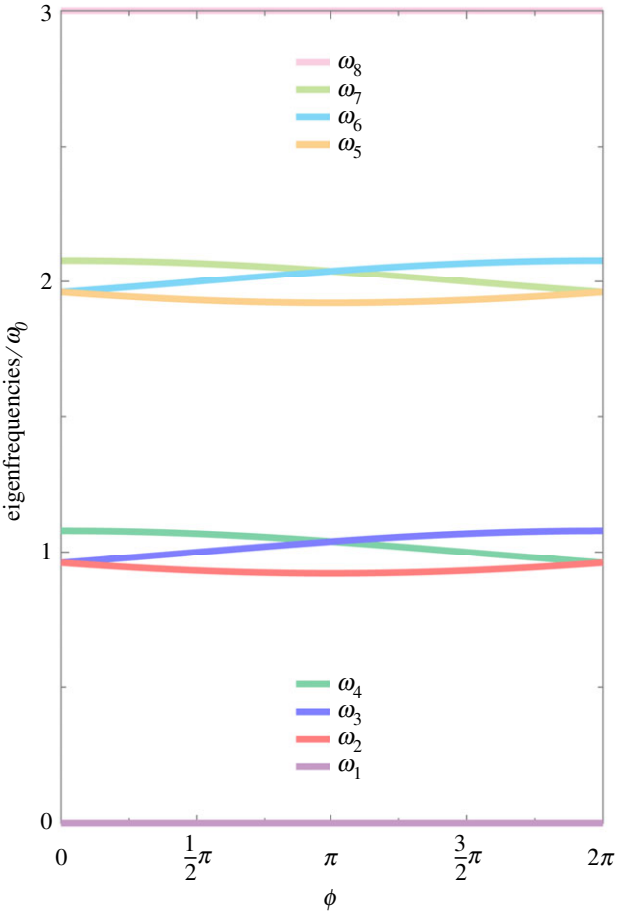

Figure 2. The eight eigenfrequencies ω_n of the trimer (in units of ω_0) in the coupled regime, as a function of the accumulated phase ϕ (see equations (2.4), (2.5) and (2.7)). In the figure, the coherent coupling strength $g = \omega_0/25$. (Online version in colour.)

system reads [66]

$$\partial_t \rho = \mathrm{i}[\rho, \hat{H}] + \sum_{n=1,2,3} \frac{\gamma_n}{2} \mathcal{L}\sigma_n + \sum_{n=1,2,3} \frac{P_n}{2} (\mathcal{L}\sigma_n)^\dagger, \tag{2.8}$$

where the Hamiltonian operator $\hat{H}$ is given by equation (2.1), and where we have used the following super-operators in Lindblad form:

$$\mathcal{L}\sigma_n = 2\sigma_n \rho \sigma_n^\dagger - \sigma_n^\dagger \sigma_n \rho - \rho \sigma_n^\dagger \sigma_n \tag{2.9}$$

and

$$(\mathcal{L}\sigma_n)^\dagger = 2\sigma_n^\dagger \rho \sigma_n - \sigma_n \sigma_n^\dagger \rho - \rho \sigma_n \sigma_n^\dagger. \tag{2.10}$$

Here $\gamma_n \geq 0$ is the damping decay rate of each individual 2LS, and $P_n \geq 0$ is the incoherent pumping rate into 2LS-n. In equation (2.8), the first term on the right-hand side is responsible for the unitary evolution (the von Neumann equation), and the second term accounts for losses into heat baths. The third term in equation (2.8) describes gain processes, so that the master equation can model both a normally ordered system and a variety of inverted systems. The formal structure of equation (2.8) is tantamount to the Gorini–Kossakowski–Sudarshan–Lindblad (GKSL) equation, which has remarkable utility across quantum optics and atomic and condensed matter physics, as reconfirmed by recent experiments. For example, Barredo and co-workers

studied blockade-type phenomena in coupled Rydberg atoms [67], where dissipators in the form of equation (2.9) sufficiently captured the effects of atomic losses due to spontaneous emission (in this experiment, the coupling $g \simeq 5\,\mathrm{MHz}$ and the loss $\gamma_n \simeq 0.3\,\mathrm{MHz}$). Furthermore, the quantum nature of evanescently coupled optical waveguides satisfying parity–time symmetry was investigated by Klauck and colleagues [68], who modelled waveguide loss well by a GKSL master equation (in this experiment, $g \simeq 49\,\mathrm{GHz}$ and $\gamma_n \simeq 38\,\mathrm{GHz}$). The aforementioned experiment of Roushan and co-workers—that with a trio of superconducting qubits—may be characterized by the parameters $g \simeq 4\,\mathrm{MHz}$ and $\gamma_n \simeq 0.1\,\mathrm{MHz}$ [23].

In what follows, we shall be interested in the interplay between non-reciprocity in transport, whose emergence has already been hinted at by the eigenfrequencies of equations (2.4) and (2.7) becoming sensitive to the gauge-independent phase ϕ, and the loss and gain in the open quantum system, which can be controlled through the parameters γ_n and P_n, respectively.

3. Chiral steady states

The non-reciprocity of the trimer system first manifests itself at the level of the steady-state populations of the collection of 2LSs. In this section, we characterize the asymmetries in the steady-state populations and steady-state currents, as a function of the accumulated phase ϕ in the system (see equation (2.5)). We relegate the calculations to the electronic supplementary material.

We consider the trimer in the set-up sketched in figure 3, with equal damping rates γ_0 ($\gamma_n = \gamma_0$, where $n = \{1, 2, 3\}$) (purple arrows in the figure), and of non-zero pumping rate P_1 into 2LS-1 (yellow arrow), while the other pumping rates are zero ($P_2 = P_3 = 0$). We show the resultant steady-state populations in figure 4 for the accumulated phase $\phi = \{0, \pi/4, \pi/2\}$ in the {left, middle, right} panels. Therefore, we can see the standard situation when $\phi = 0$, and two example non-reciprocal cases when $\phi = \{\pi/4, \pi/2\}$. In the top (bottom) panels, the magnitude of the coherent coupling $g = \gamma_0$ ($g = 5\gamma_0$). The labelling of the mean population of the state $|i, j, k\rangle$ is displayed in the legend of figure 4*a*, and states with $N = \{0, 1, 2, 3\}$ excitations are shown with increasingly thick lines.

Let us start by considering figure 4*a*, where the phase $\phi = 0$. The fine purple line corresponds to the mean population of the ground state $|0, 0, 0\rangle$, which is the only possible state at vanishing pumping $P_1 \ll \gamma_0$, and it monotonically decreases with increasing pumping rate P_1, since the non-trivial states become populated. The results for the set of single-excitation states are given by the thin lines, and comprise the mean populations of the states $|1, 0, 0\rangle$, $|0, 1, 0\rangle$ and $|0, 0, 1\rangle$, which are denoted by green, blue and red lines, respectively. Since only 2LS-1 is being pumped, the $|1, 0, 0\rangle$ population (green line) grows quickly with increasing pumping rate P_1, and approaches unity within the large pump limit $P_1 \gg \gamma_0$. Meanwhile, the populations of the states $|0, 1, 0\rangle$ and $|0, 0, 1\rangle$ (blue and red lines, respectively) are identical owing to the absence of any accumulated phase ϕ, and they form a hump structure since they are not populated in the low or high pump limits. The results for the set of two-excitation states are given by the medium thickness lines, and comprise the mean populations of the states $|1, 1, 0\rangle$, $|1, 0, 1\rangle$ and $|0, 1, 1\rangle$, which are denoted by orange, cyan and lime lines, respectively. The mean populations of the states $|1, 1, 0\rangle$ and $|1, 0, 1\rangle$ (orange and cyan lines, respectively) are the same, forming a hump structure peaked at a higher pumping rate than the single-excitation populations of $|0, 1, 0\rangle$ and $|0, 0, 1\rangle$. As only 2LS-1 is being fed with gain, the $|0, 1, 1\rangle$ mean population (lime line) is negligible, as is the mean population of the triply excited state $|1, 1, 1\rangle$, which is represented by the thick pink line. This panel exemplifies the standard reciprocal situation, without any asymmetries or surprises.

In figure 4*b*, we have a non-trivial accumulated phase $\phi = \pi/4$. The effect is to break two symmetries in the steady-state populations. In the single-excitation subspace, the populations of the states $|0, 1, 0\rangle$ and $|0, 0, 1\rangle$ (blue and red lines, respectively) are no longer identical (see figure 4*a*). Similarly, in the two-excitation subspace, the populations of the states $|1, 1, 0\rangle$ and $|1, 0, 1\rangle$ (orange and cyan lines, respectively) are now noticeably different. These asymmetries are the hallmark of non-reciprocity in the trimer system, as caused by the directionality imposed by

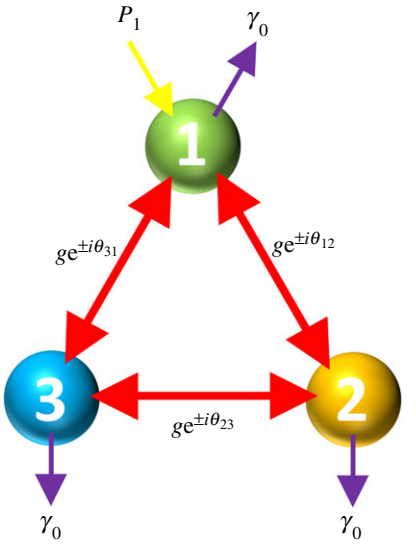

Figure 3. A sketch of the trimer with specific parameter choices (see equations (2.1) and (2.8)). Each 2LS is of resonance frequency ω_0 and damping rate γ_0 (purple arrows). The 2LS-1 is subject to gain at a rate P_1 (yellow arrow), while $P_2 = P_3 = 0$. The magnitude of the three coherent coupling constants is g, and the hopping between sites n and $n+1$ is augmented with the complex argument θ_{nn+1}. (Online version in colour.)

the non-zero phase ϕ. In figure 4*c*, the accumulated phase is increased to $\phi = \pi/2$, showcasing further population imbalances in both the first and second rung of the energy ladder, in a manifestation of multi-excitation Aharonov–Bohm physics. Notably, if we were to further consider $\phi = 3\pi/2$, the result would effectively be the opposite of that in figure 4*c*, where $\phi = \pi/2$. That is, the populations of $|0,1,0\rangle$ and $|0,0,1\rangle$ would be reversed, and those of $|1,1,0\rangle$ and $|1,0,1\rangle$ would also be reversed, with respect to figure 4*c*.

In figure 4*d–f*, the magnitude of the coherent coupling is increased to $g = 5\gamma_0$ (in figure 4*a–c*, $g = \gamma_0$). This stronger coupling leads to a significantly richer structure of the mean populations of the system, since the doubly and triply excited states have more chances to be populated. Figure 4*d* shows the reciprocal case with $\phi = 0$, where there is a clear region of large population inversion. Indeed the triply excited state $|1,1,1\rangle$ has the most chance of being excited approximately within $10\gamma_0 < P_1 < 100\gamma_0$ (thick pink line). Non-reciprocity appears in figure 4*e,f*, where $\phi = \pi/4$ and $\phi = \pi/2$, respectively, and where two population symmetries have been broken in the same manner as in figure 4*b,c*. That is, the $N = 1$ excitation mean populations (red and blue lines) and the $N = 2$ excitation mean populations (orange and cyan lines), which coincide in figure 4*d*, are now completely distinguishable in figure 4*e,f*.

Perhaps surprisingly, figure 4*e,f* also showcases a region in which the population of 2LS-3 is greater than that of 2LS-2, an area which is bordered by the thin vertical lines. Primarily, this inversion is because of the population of $|1,0,1\rangle$ (cyan lines) being greater than the population of $|1,1,0\rangle$ (orange lines) for moderate ratios of P_1/γ_0, where the system is mostly in the two-excitation sector. Outside of this moderate pumping region, one sees that for low pumping $P_1 \lessapprox \gamma_0$, where the system is mostly in the one-excitation sector, 2LS-2 is more excited than 2LS-3, owing to the population of $|0,1,0\rangle$ (blue lines) being greater than the population of $|0,0,1\rangle$ (red lines). Similarly, for large pumping $P_1 \gg \gamma_0$ the population imbalance is also in favour of 2LS-2, as guaranteed by the population of $|1,1,0\rangle$ (orange lines) being greater than the population of $|1,0,1\rangle$ (cyan lines). The populations of each individual 2LS, rather than those of the states $|i,j,k\rangle$, can be explicitly seen in the electronic supplementary material, figure S1. Most

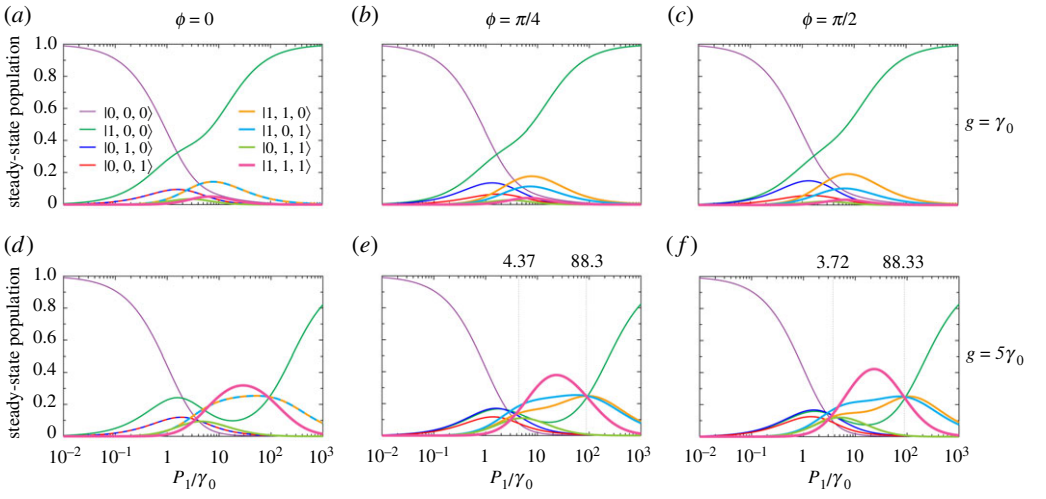

Figure 4. Steady-state populations in the trimer as a function of the pumping rate P_1 into 2LS-1, in units of the common decay rate γ_0 (see the configuration in figure 3). The other pumping rates are zero ($P_2 = P_3 = 0$). We show results for the accumulated phase $\phi = \{0, \pi/4, \pi/2\}$ in the {left, middle, right} panels. Top (bottom) panels: the magnitude of the coherent coupling $g = \gamma_0$ ($g = 5\gamma_0$). The labelling of the mean population of the state $|i, j, k\rangle$ is displayed in the legend in (*a*), and states with $N = \{0, 1, 2, 3\}$ excitations are shown with increasingly thick lines. Thin, vertical lines in (*e*,*f*): guides for the eye at the ratios of P_1/γ_0, which form a region in which 2LS-3 is more populated than 2LS-2. (Online version in colour.)

notably, the region of inverted population imbalance only occurs within the thin vertical lines in figure 4*e*,*f*, since it requires both a non-trivial accumulated phase ϕ and a sufficiently strong coupling g.

An important observable to consider is the steady-state current across the three sites of the trimer. To do so, let us consider the continuity equation at each site n,

$$\partial_t(\sigma_n^\dagger \sigma_n) = \mathrm{i}[\sigma_n^\dagger \sigma_n, \hat{H}] = I_{nn+1} - I_{n-1n}, \tag{3.1}$$

where the Hamiltonian operator $\hat{H}$ is given by equation (2.1). In equation (3.1), we have introduced the local current operator I_{nn+1}, describing the transfer of excitations between two neighbouring sites n and $n+1$ in the trimer (we assume modular arithmetic for the indices), as

$$I_{nn+1} = \mathrm{i}g(\mathrm{e}^{\mathrm{i}\theta_{nn+1}}\sigma_n^\dagger \sigma_{n+1} - \mathrm{e}^{-\mathrm{i}\theta_{nn+1}}\sigma_{n+1}^\dagger \sigma_n). \tag{3.2}$$

The global current operator I naturally follows as

$$I = I_{12} + I_{23} + I_{31}, \tag{3.3}$$

and we donate the mean versions of these quantities as

$$J = \langle I \rangle \tag{3.4a}$$

and

$$J_{nn+1} = \langle I_{nn+1} \rangle. \tag{3.4b}$$

The steady-state (ss) versions of these quantities, J^{ss} and J^{ss}_{nn+1}, portray how the excitations in the system are transferred at large time scales. The results are presented in figure 5*a*,*b*, as a function of the pumping rate P_1 into 2LS-1. We show results for the accumulated phase $\phi = \{0, \pi/4, \pi/2\}$ with increasingly thin lines, and in the left (right)-hand panels the magnitude of the coherent coupling $g = \gamma_0$ ($g = 5\gamma_0$). Figure 5*a* highlights the absence of a steady-state current when $\phi = 0$ (thick green line). When $\phi = \pi/4$ (medium pink line), a non-zero steady-state current is able to be supported because of the population imbalance between 2LS-2 and 2LS-3, and it has a maximal

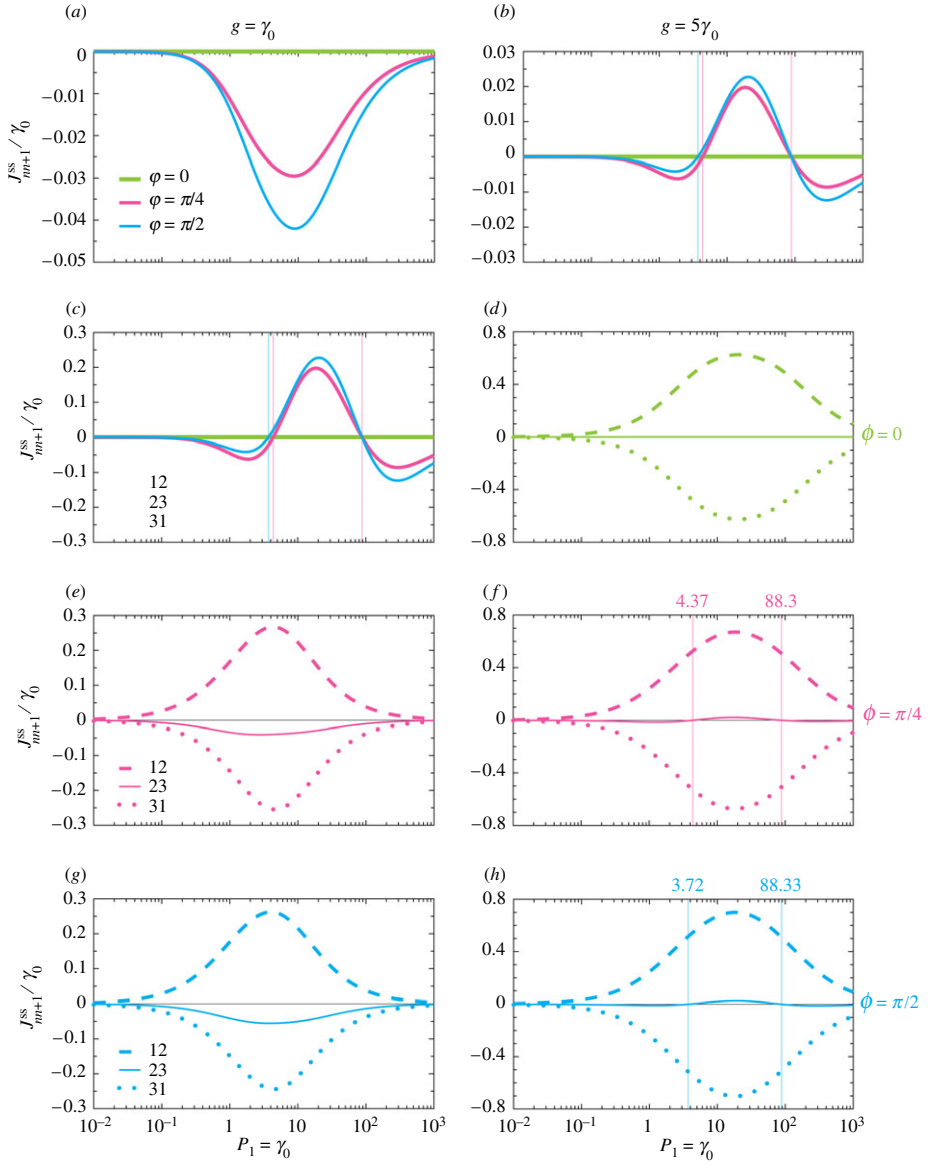

Figure 5. (*a*,*b*) Global steady-state current J^{ss} in the trimer, as a function of the pumping rate P_1 into 2LS-1, in units of the common decay rate γ_0 (see the configuration in figure 3). The other pumping rates are zero ($P_2 = P_3 = 0$). We show results for the accumulated phases $\phi = \{0, \pi/4, \pi/2\}$ with increasingly thin lines. (*c*–*h*) Local currents J^{ss}_{nn+1} for the three phases ϕ corresponding to (*a*,*b*) (see equation (3.4)). The dashed, solid and dotted lines represent J^{ss}_{12}, J^{ss}_{23} and J^{ss}_{31}, respectively. Thin vertical lines: guides for the eye at the ratio of P_1/γ_0 corresponding to sign changes of the global steady-state current J^{ss}. Left (right)-hand panels: the magnitude of the coherent coupling $g = \gamma_0$ ($g = 5\gamma_0$). (Online version in colour.)

value around $P_1 \simeq 10\gamma_0$. The case of $\phi = \pi/2$ (thin cyan line) displays the greatest steady-state current, as follows from figure 4*c*,*f*, where the mean population asymmetries are also greatest.

In figure 5*b*, the effect of increased coherent coupling g leads to a notably different behaviour. While the reciprocal case current remains zero (thick green line), and the currents in the non-reciprocal cases (thinner lines) remain zero in the limiting cases of vanishing pumping and large pumping (these asymptotics are guaranteed from figure 4, because of saturation), the intermediate behaviour is more interesting. The steady-state current J^{ss} becomes a sign-changing

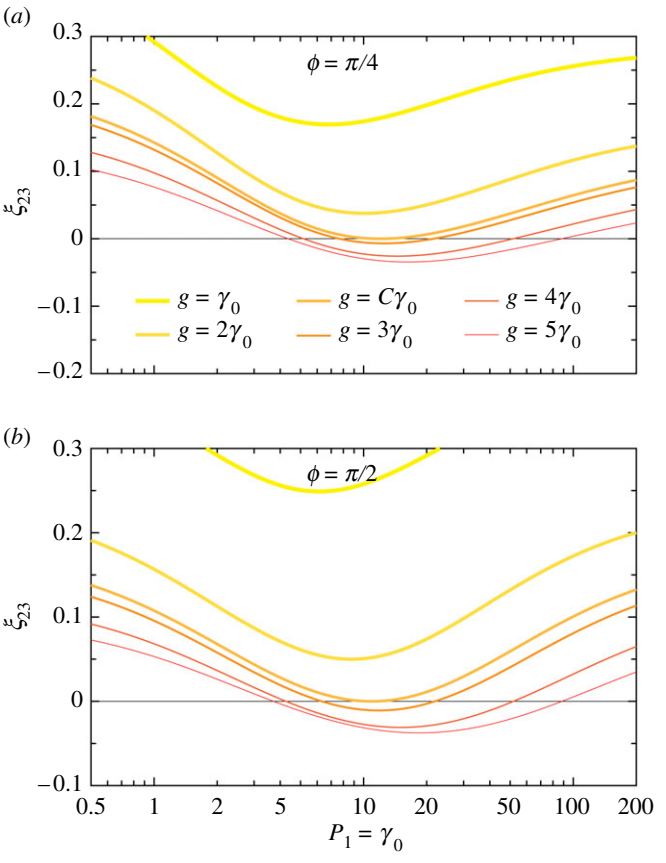

Figure 6. Population imbalance ξ_{23} between 2LS-2 and 2LS-3 in the steady state, as a function of the pumping rate P_1 into 2LS-1, in units of the common decay rate γ_0 (see equation (3.5)). The other pumping rates are zero ($P_2 = P_3 = 0$). We show results for increasingly strong coherent coupling strengths g with increasingly thin and dark lines. In (*a*) ((*b*)) the accumulated phase $\phi = \pi/4$ ($\phi = \pi/2$), and the phase-dependent constant $C = 2.72$ ($C = 2.77$) is associated with the smallest ratio of g/γ_0 at which ξ_{23} may cross zero. (Online version in colour.)

quantity with a varying pumping rate, owing to multi-excitation effects. As can be seen from figure 4*d–f*, the higher coupling g allows for states beyond the single-excitation sector to become significantly populated, and for the population of 2LS-3 to be higher than that of 2LS-2 for certain regions in figure 4*e,f*, that is, inside the thin vertical lines. In figure 5*b*, this population inversion leads to a breakdown of the single-signed steady-state current behaviour showcased in figure 5*a*, suggesting that it is not simply the phase ϕ which governs the directionality.

Figure 5*c–h* shows the constituent local steady-state currents J^{ss}_{nn+1}, between two consecutive sites n and $n+1$. Figure 5*c* makes explicit how there is no global current when $\phi = 0$, since the J_{12} and J_{31} local steady-state currents (dashed and dotted lines) are exactly opposite because of the reciprocal coupling. In figure 5*e,g*, where $\phi = \pi/4$ and $\phi = \pi/2$, respectively, the non-reciprocal nature of the coupling leads to a non-zero component J_{23} (solid lines), which engenders the global current result shown in figure 5*a*. In figure 5*b,d,f,h*, where the coherent coupling strength g is stronger, some differences may be observed in the non-trivial phase cases, as shown in figure 5*f,h*. Principally, J_{23} becomes a sign-changing quantity at certain pumping rates (marked by the thin vertical lines) owing to the population imbalance between 2LS-2 and 2LS-3. This leads directly to the corresponding global current sign-changing behaviour, as is shown in figure 5*b*.

In order to examine the sign change in J_{23} in more detail, we define the steady-state (ss) population imbalance between 2LS-2 and 2LS-3,

$$\xi_{23} = \frac{\langle \sigma_2^\dagger \sigma_2 \rangle_{\rm ss} - \langle \sigma_3^\dagger \sigma_3 \rangle_{\rm ss}}{\langle \sigma_2^\dagger \sigma_2 \rangle_{\rm ss} + \langle \sigma_3^\dagger \sigma_3 \rangle_{\rm ss}}. \tag{3.5}$$

We plot this population imbalance ξ_{23} in figure 6, as a function of the pumping rate P_1 into 2LS-1. We show results for increasingly strong coherent coupling strengths g with increasingly thin and dark lines. In figure 6*a*, where the accumulated phase $\phi = \pi/4$, one notices $\xi_{23} > 0$ (for all P_1) for weaker couplings g (thicker, brighter lines). When the critical strength $C = 2.72$ is reached (medium orange line), ξ_{23} may first touch zero for some value of P_1. For stronger couplings (thinner, darker lines), the inverted population imbalance $\xi_{23} < 0$ becomes apparent for intermediate pumping regimes, leading to the sign-changing current shown in figure 5*f*. In figure 6*b*, where $\phi = \pi/2$, the same qualitative behaviour is displayed. The most prominent differences are an increase in the critical strength to $C = 2.77$, and changes in the ranges of the regions of pumping supporting inverted population imbalances ($\xi_{23} < 0$), explaining the sign-changing current shown in figure 5*h*. Taken together, figures 4 and 5 provide an atlas describing how non-reciprocity can be observed once a pumped system has reached its steady state. Importantly, it goes beyond the single-excitation limit, and shows how asymmetries arise in both singly and doubly excited manifolds, which can lead to an interesting sign-changing behaviour of the formed chiral steady-state currents, as demonstrated in figure 6.

4. Non-reciprocal dynamics

The impact of the accumulated phase ϕ in the triangular cluster of 2LSs is also felt in the population dynamics, which gives rise to dynamic chiral currents. In this section, we investigate the transient population and current in the trimer, in the configuration sketched in figure 3 and used throughout §3. We leave the supporting calculations to the electronic supplementary material.

In figure 7, we show the behaviour of the mean populations $\langle \sigma_n^\dagger \sigma_n \rangle$ of 2LS-n as a function of time t, in units of the inverse decay rate γ_0^{-1}. We display results for the phases $\phi = \{0, \pi/4, \pi/2\}$, corresponding to one reciprocal and two non-reciprocal cases, in the left, middle and right columns. We consider weak ($P_1 = \gamma_0/10$), moderate ($P_1 = \gamma_0$) and strong ($P_1 = 10\gamma_0$) pumping into 2LS-1 in the top, middle and bottom rows, respectively. The magnitudes of the coherent coupling $g = 5\gamma_0$ and the other pumping rates are zero ($P_2 = P_3 = 0$). These parameter choices correspond to figure 4*d–f* in §3. Reciprocal population dynamics is clearly observed in figure 7*a*, where the phase $\phi = 0$, since the populations of 2LS-2 (orange line) and 2LS-3 (cyan line) are equivalent. In figure 7*b*, there is a non-trivial phase of $\phi = \pi/4$ in the trimer, which causes a breakdown of the aforementioned equivalence, such that some directionality starts to appear in the system. Figure 7*c* presents the most obviously directional circulation, 2LS-1 → 2LS-2 → 2LS-3 (lime → orange → cyan), which corresponds to the special phase $\phi = \pi/2$.

Let us now consider the influence of higher pumping rates by looking at figure 7*d–f*, where $P_1 = \gamma_0$. Figure 7*d* illustrates the reciprocal case ($\phi = 0$), which notably reaches its steady-state behaviour faster than in figure 7*a*, since the gain dominates the coherent coupling g sooner. In figure 7*e*, the non-trivial phase $\phi = \pi/4$ breaks the equivalence of 2LS-2 and 2LS-3, but the directionality is less pronounced than in figure 7*b*. This is because the extra gain has led to higher rungs of the energy ladder becoming populated (see figure 1*b*), blurring the population cycles. An explicit plot tracking the transient population of each individual state $|i, j, k\rangle$ is given in the middle row of panels in electronic supplementary material, figure S2, illustrating this fact. The spoiling of the asymmetric population transfer is most evident in figure 7*f*, where $\phi = \pi/2$. In stark contrast to figure 7*c*, in figure 7*f* there are only a few directional population cycles before the steady state is reached because of the dominant pumping rate.

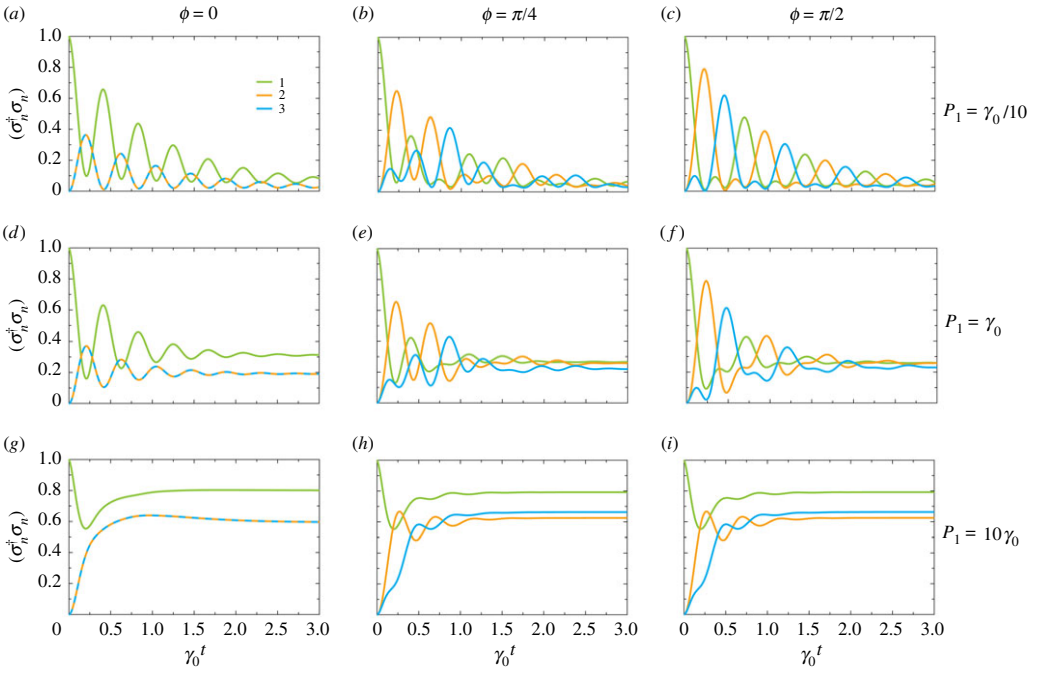

Figure 7. Population dynamics in the trimer as a function of time t, in units of the inverse decay rate γ_0^{-1} (see the configuration in figure 3). The population $\langle\sigma_n^\dagger\sigma_n\rangle$ of 2LS-n is denoted in the legend in (*a*). The magnitude of the coherent coupling $g = 5\gamma_0$, two of the pumping rates are zero ($P_2 = P_3 = 0$) and the initial condition at $t = 0$ is the state $|1, 0, 0\rangle$. We show results for the accumulated phase $\phi = \{0, \pi/4, \pi/2\}$ in the {left, middle, right} columns. (*a–c*) Weak pumping into the first 2LS, $P_1 = \gamma_0/10$. (*d–f*) Moderate pumping, $P_1 = \gamma_0$. (*g–i*) Strong pumping, $P_1 = 10\gamma_0$. (Online version in colour.)

We investigate the limiting case of large pumping in figure 7*g–i*, where $P_1 = 10\gamma_0$. The reciprocal coupling case in figure 7*g* highlights that the large amount of gain in the system washes out any population cycles. The same effect is seen for the non-reciprocal cases, in figure 7*h,i*, respectively, where the high pumping rate sees the second and third excitation manifolds quickly become populated and the steady state reached (see figure 4*e,f*), without any chance for meaningful directional circulation. We explicitly show how each individual state $|i, j, k\rangle$ behaves in the lower row of panels in the electronic supplementary material, figure S1.

The global current J around the trimer measures the dynamic transfer of excitations in the looped system. The results are presented in figure 8*a–c*, where the magnitude of the coherent coupling remains at $g = 5\gamma_0$. The accumulated phase $\phi = \{0, \pi/4, \pi/2\}$ is denoted by increasingly thin lines. The left, central and right columns describe weak ($P_1 = \gamma_0/10$), moderate ($P_1 = \gamma_0$) and strong ($P_1 = 10\gamma_0$) pumping rates, respectively. Common across figure 8*a–c* is the absence of any global current J when $\phi = 0$ (thick green lines), since the system is completely reciprocal in this circumstance. Meanwhile, the non-reciprocal cases of $\phi = \pi/4$ and $\phi = \pi/2$ (medium pink and thin cyan lines, respectively) display non-trivial global currents along figure 8*a–c* owing to the population imbalance in the system. In the low pumping case of figure 8*a*, the non-reciprocal angle cases display chiral currents over several population cycles, in line with figure 7*a–c*. With moderate pumping in figure 8*b*, the waveform is similar to that in figure 8*a*, although the magnitude of the current is larger. However in figure 8*c*, where the pumping is strong, a significant differences emerges. Similar to figure 7*d–i*, the high pumping rate sees the steady-state current J^{ss} be reached quickly.

Figure 8*d–l* shows the constituent local currents J_{nn+1} between two successive sites n and $n + 1$. Let us consider figure 8*d–f*, where the accumulated phase is trivial $\phi = 0$. The inherent reciprocity ensures that the local currents J_{12} (dashed green lines) and J_{31} (dotted green lines) are equal

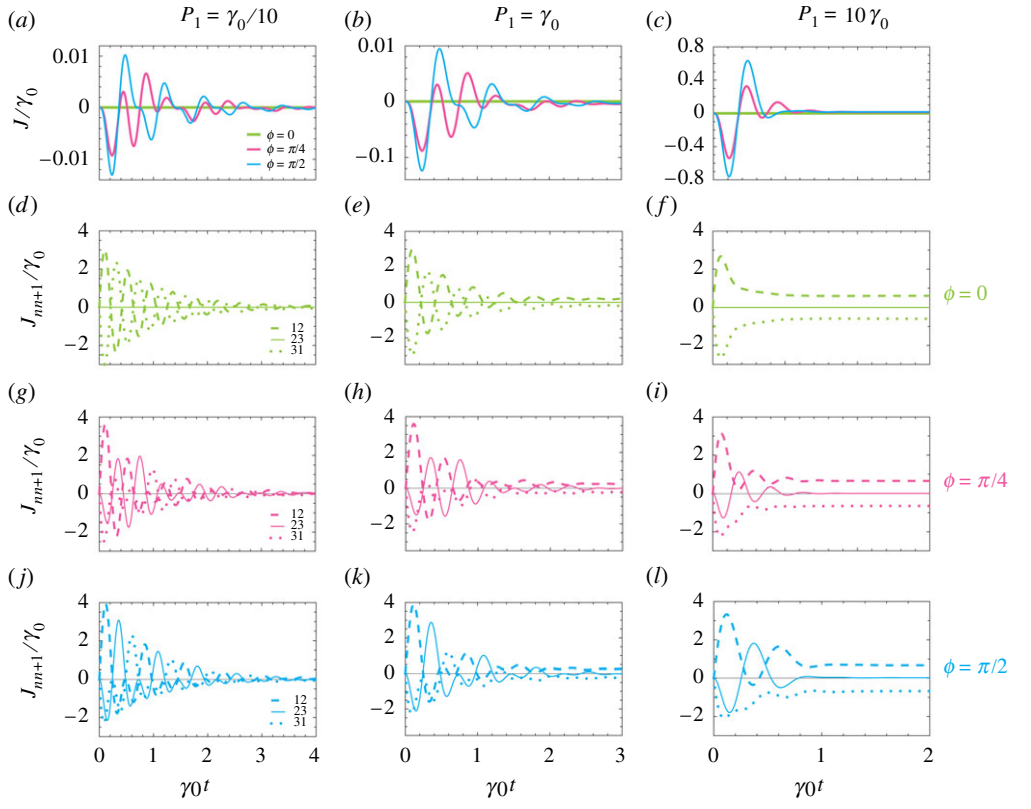

Figure 8. (*a–c*) Global current J in the trimer as a function of time t, in units of the inverse decay rate γ_0^{-1} (see the configuration in figure 3). The magnitude of the coherent coupling $g = 5\gamma_0$, two of the pumping rates are zero ($P_2 = P_3 = 0$) and the initial condition at $t = 0$ is the state $|1, 0, 0\rangle$. We show results for the accumulated phase $\phi = \{0, \pi/4, \pi/2\}$ with increasingly thin lines. (*d–l*) Local currents J_{nn+1} for the three phases ϕ corresponding to (*a–c*) (see equation (3.4)). The dashed, solid and dotted lines represent J_{12}, J_{23} and J_{31}, respectively. (*a,d,g,j*) Weak pumping into the first 2LS, $P_1 = \gamma_0/10$. (*b,e,h,k*) Moderate pumping, $P_1 = \gamma_0$. (*c,f,i,l*) Strong pumping, $P_1 = 10\gamma_0$. (Online version in colour.)

and opposite, leading to their exact cancellation, while J_{23} (solid green lines) is consequentially zero. In figure 8*g–i*, there is a non-trivial phase $\phi = \pi/4$. This non-reciprocity results in a non-zero local current J_{23} (solid pink lines), leading to a noticeable global current J. Going across figure 8*g–i*, the impact of higher pumping rates is to see the steady states be reached sooner, quenching the dynamic current cycles. Figure 8*j–l*, where $\phi = \pi/2$, shows similar behaviour, but the increased non-reciprocity leads to higher directional circulation and so larger amplitudes in the current cycles. Collectively, figures 7 and 8 exhibit how dynamic directional circulation arises in a trimer of 2LSs for a range of strengths of incoherent pumping and accumulated phases, and takes account of effects beyond the single-excitation limit. This demonstration has implications for the optimal design of non-reciprocal devices built from more complicated arrays of meta-atoms, particularly with regard to the balance of gain and losses.

5. Discussion

We have considered a trimer of 2LSs in an open quantum systems approach, where both the magnitude and phase of the coherent coupling constants are important. Including losses and gain via a quantum master equation, we have calculated the mean populations of all of the possible states in the system, beyond the single-excitation sector. Remarkably, for non-trivial accumulated phases, the mean populations have a non-reciprocal character in both the transient and steady

states, in a manifestation of an Aharonov–Bohm-like effect. The non-reciprocity is exemplified by population imbalances of both singly and doubly excited states, leading to the formation of chiral currents both dynamically and in the steady state. Perhaps surprisingly, in addition to the accumulated phase in the loop, the sign of the population imbalance may also be controlled by the coupling strength and the amount of gain in the system, which determined the direction of the current.

The presented (and rather general) theory paves the way for the experimental detection of chiral currents in trimers of meta-atoms in the latest quantum metamaterials, including with photonic [69–72] and plasmonic [73–76] excitations, as well as with circuit QED platforms [77–79], clusters of ions [80], and Rydberg [81,82] and ultracold [83–86] atoms. The tantalizing prospect of the realization of a building block of future non-reciprocal nanophotonic circuitry, such as a circulator or isolator [15–22], is within reach.

Data accessibility. All of the information required to reproduce the paper is contained within the paper and the electronic supplementary material.

Authors' contributions. C.A.D. performed the calculations and wrote the first version of the manuscript. D.Z. conceived of the study, supervised the project and helped to draft the manuscript. Both authors gave final approval for publication and agree to be held accountable for the work performed therein.

Competing interests. We declare we have no competing interests.

Funding. C.A.D. is supported by a Royal Society University Research Fellowship (URF/R1/201158), and via a Royal Society Research Grant (RGS/R1/211220). D.Z. is supported by the Spanish Government (grant no. PID2020-115221GBC41/AEI/10.13039/501100011033), the Gobierno de Aragón (grant no. E09-17R Q-MAD) and the CSIC Quantum Technologies Platform PTI-001.

Acknowledgements. We thank L. Martín-Moreno for fruitful conversations.

References

1. Trivers RE. 1971 The evolution of reciprocal altruism. *Q. Rev. Biol.* **46**, 35–57. (doi:10.1086/406755)
2. Maynard Smith J. 1982 *Evolution and the theory of games*. Cambridge, UK: Cambridge University Press.
3. Tame MS, McEnery KR, Ozdemir SK, Lee J, Maier SA, Kim MS. 2013 Quantum plasmonics. *Nat. Phys.* **9**, 329–340. (doi:10.1038/nphys2615)
4. Keimer B, Moore JE. 2017 The physics of quantum materials. *Nat. Phys.* **13**, 1045–1055. (doi:10.1038/nphys4302)
5. O'Brien J, Furusawa A, Vuckovic J. 2009 Photonic quantum technologies. *Nat. Photonics* **3**, 687–695. (doi:10.1038/nphoton.2009.229)
6. Wang J, Sciarrino F, Laing A, Thompson MG. 2019 Integrated photonic quantum technologies. *Nat. Photonics* **14**, 273–284. (doi:10.1038/s41566-019-0532-1)
7. Meinzer N, Barnes WL, Hooper IR. 2014 Plasmonic meta-atoms and metasurfaces. *Nat. Photonics* **8**, 889–898. (doi:10.1038/nphoton.2014.247)
8. Chang DE, Douglas JS, Gonzalez-Tudela A, Hung C-L, Kimble HJ. 2018 Colloquium: quantum matter built from nanoscopic lattices of atoms and photons. *Rev. Mod. Phys.* **90**, 031002. (doi:10.1103/RevModPhys.90.031002)
9. Bekenstein R, Pikovski I, Pichler H, Shahmoon E, Yelin SF, Lukin MD. 2020 Quantum metasurfaces with atom arrays. *Nat. Phys.* **16**, 676–681. (doi:10.1038/s41567-020-0845-5)
10. Martinez Azcona P, Downing CA. 2021 Doublons, topology and interactions in a one-dimensional lattice. *Sci. Rep.* **11**, 12540. (doi:10.1038/s41598-021-91778-z)
11. Lodahl P, Mahmoodian S, Stobbe S, Rauschenbeutel A, Schneeweiss P, Volz J, Pichler H, Zoller P. 2017 Chiral quantum optics. *Nature* **541**, 473–480. (doi:10.1038/nature21037)
12. Andrews DL. 2018 Quantum formulation for nanoscale optical and material chirality: symmetry issues, space and time parity, and observables. *J. Opt.* **20**, 033003. (doi:10.1088/2040-8986/aaaa56)
13. Ozawa T *et al.* 2019 Topological photonics. *Rev. Mod. Phys.* **91**, 015006. (doi:10.1103/RevModPhys.91.015006)
14. Ozawa T, Price HM. 2019 Topological quantum matter in synthetic dimensions. *Nat. Rev. Phys.* **1**, 349–357. (doi:10.1038/s42254-019-0045-3)

15. Jalas D *et al.* 2013 What is—and what is not—an optical isolator. *Nat. Photonics* **7**, 579–582. (doi:10.1038/nphoton.2013.185)
16. Sollner I *et al.* 2015 Deterministic photon-emitter coupling in chiral photonic circuits. *Nat. Nanotech.* **10**, 775–778. (doi:10.1038/nnano.2015.159)
17. Sayrin C, Junge C, Mitsch R, Albrecht B, O'Shea D, Schneeweiss P, Volz J, Rauschenbeutel A. 2015 Nanophotonic optical isolator controlled by the internal state of cold atoms. *Phys. Rev. X* **5**, 041036. (doi:10.1103/PhysRevX.5.041036)
18. Scheucher M, Hilico A, Will E, Volz J, Rauschenbeutel A. 2016 Quantum optical circulator controlled by a single chirally coupled atom. *Science* **354**, 1577–1580. (doi:10.1126/science.aaj2118)
19. Barzanjeh S, Wulf M, Peruzzo M, Kalaee M, Dieterle PB, Painter O, Fink JM. 2017 Mechanical on-chip microwave circulator. *Nat. Commun.* **8**, 953. (doi:10.1038/s41467-017-01304-x)
20. Shen Z, Zhang Y-L, Chen Y, Sun F-W, Zou X-B, Guo G-C, Zou C-L, Dong C-H. 2018 Reconfigurable optomechanical circulator and directional amplifier. *Nat. Commun.* **9**, 1797. (doi:10.1038/s41467-018-04187-8)
21. Ruesink F, Mathew JP, Miri M-A, Alu A, Verhagen E. 2018 Optical circulation in a multimode optomechanical resonator. *Nat. Commun.* **9**, 1798. (doi:10.1038/s41467-018-04202-y)
22. Zhang S, Hu Y, Lin G, Niu Y, Xia K, Gong J, Gong S. 2018 Thermal-motion-induced non-reciprocal quantum optical system. *Nat. Photonics* **12**, 744–748. (doi:10.1038/s41566-018-0269-2)
23. Roushan P *et al.* 2017 Chiral ground-state currents of interacting photons in a synthetic magnetic field. *Nat. Phys.* **13**, 146–151. (doi:10.1038/nphys3930)
24. Roy D, Wilson CM, Firstenberg O. 2017 Colloquium: strongly interacting photons in one-dimensional continuum. *Rev. Mod. Phys.* **89**, 021001. (doi:10.1103/RevModPhys.89.021001)
25. Xue Z-Y, Hu Y. 2021 Topological photonics on superconducting quantum circuits with parametric couplings. *Adv. Quantum Technol.* **4**, 2100017. (doi:10.1002/qute.202100017)
26. Harper PG. 1955 The general motion of conduction electrons in a uniform magnetic field, with application to the diamagnetism of metals. *Proc. Phys. Soc. A* **68**, 879. (doi:10.1088/0370-1298/68/10/305)
27. Hofstadter DR. 1976 Energy levels and wave functions of Bloch electrons in rational and irrational magnetic fields. *Phys. Rev. B* **14**, 2239–2249. (doi:10.1103/PhysRevB.14.2239)
28. Haldane FDM. 1988 Model for a quantum Hall effect without Landau levels: condensed-matter realization of the 'parity anomaly'. *Phys. Rev. Lett.* **61**, 2015–2018. (doi:10.1103/PhysRevLett.61.2015)
29. Fang K, Yu Z, Fan S. 2012 Realizing effective magnetic field for photons by controlling the phase of dynamic modulation. *Nat. Photonics* **6**, 782–787. (doi:10.1038/nphoton.2012.236)
30. Sanchez-Burillo E, Wan C, Zueco D, Gonzalez-Tudela A. 2020 Chiral quantum optics in photonic sawtooth lattices. *Phys. Rev. Res.* **2**, 023003. (doi:10.1103/PhysRevResearch.2.023003)
31. Celi A, Massignan P, Ruseckas J, Goldman N, Spielman IB, Juzeliunas G, Lewenstein M. 2014 Synthetic gauge fields in synthetic dimensions. *Phys. Rev. Lett.* **112**, 043001. (doi:10.1103/PhysRevLett.112.043001)
32. Lin Y-J, Compton RL, Jimenez-Garcia K, Porto JV, Spielman IB. 2009 Synthetic magnetic fields for ultracold neutral atoms. *Nature* **462**, 628–632. (doi:10.1038/nature08609)
33. Gunter KJ, Cheneau M, Yefsah T, Rath SP, Dalibard J. 2009 Practical scheme for a light-induced gauge field in an atomic Bose gas. *Phys. Rev. A* **79**, 011604(R). (doi:10.1103/PhysRevA.79.011604)
34. Spielman IB. 2009 Raman processes and effective gauge potentials. *Phys. Rev. A* **79**, 063613. (doi:10.1103/PhysRevA.79.063613)
35. Zhao E. 2018 Topological circuits of inductors and capacitors. *Ann. Phys.* **399**, 289–313. (doi:10.1016/j.aop.2018.10.006)
36. Downing CA, López Carreño JC, Laussy FP, del Valle E, Fernández-Domínguez AI. 2019 Quasichiral interactions between quantum emitters at the nanoscale. *Phys. Rev. Lett.* **122**, 057401. (doi:10.1103/PhysRevLett.122.057401)
37. Comaron P, Shahnazaryan V, Brzezicki W, Hyart T, Matuszewski M. 2020 Non-Hermitian topological end-mode lasing in polariton systems. *Phys. Rev. Res.* **2**, 022051(R). (doi:10.1103/PhysRevResearch.2.022051)
38. Allen L, Eberly JH. 1975 *Optical resonance and two-level atoms*. New York, NY: Wiley.
39. Wang D-W *et al.* 2019 Synthesis of antisymmetric spin exchange interaction and chiral spin clusters in superconducting circuits. *Nat. Phys.* **15**, 382–386. (doi:10.1038/s41567-018-0400-9)

40. Kjaergaard M, Schwartz ME, Braumuller J, Krantz P, Wang JIJ, Gustavsson S, Olive WD. 2020 Superconducting qubits: current state of play. *Annu. Rev. Condens. Matter Phys.* **11**, 369–395. (doi:10.1146/annurev-conmatphys-031119-050605)
41. Cooper NR, Dalibard J, Spielman IB. 2019 Topological bands for ultracold atoms. *Rev. Mod. Phys.* **91**, 015005. (doi:10.1103/RevModPhys.91.015005)
42. Bordo VG. 2019 Quantum plasmonics of metal nanoparticles. *J. Opt. Soc. Am. B* **36**, 323–332. (doi:10.1364/JOSAB.36.000323)
43. Aharonov Y, Bohm D. 1959 Significance of electromagnetic potentials in the quantum theory. *Phys. Rev.* **115**, 485–491. (doi:10.1103/PhysRev.115.485)
44. Li K, Kevrekidis PG. 2011 PT-symmetric oligomers: analytical solutions, linear stability, and nonlinear dynamics. *Phys. Rev. E* **83**, 066608. (doi:10.1103/PhysRevE.83.066608)
45. Duanmu M, Li K, Horne RL, Kevrekidis PG, Whitaker N. 2013 Linear and nonlinear parity-time-symmetric oligomers: a dynamical systems analysis. *Phil. Trans. R. Soc. A* **371**, 20120171. (doi:10.1098/rsta.2012.0171)
46. Li K, Kevrekidis PG, Frantzeskakis DJ, Ruter CE, Kip D. 2013 Revisiting the PT-symmetric trimer: bifurcations, ghost states and associated dynamics. *J. Phys. A: Math. Theor.* **46**, 375304. (doi:10.1088/1751-8113/46/37/375304)
47. Suchkov SV, Fotsa-Ngaffo F, Kenfack-Jiotsa A, Tikeng AD, Kofane TC, Kivshar YS, Sukhorukov AA. 2016 Non-Hermitian trimers: PT-symmetry versus pseudo-hermiticity. *New J. Phys.* **18**, 065005. (doi:10.1088/1367-2630/18/6/065005)
48. Suchkov SV, Sukhorukov AA, Huang J, Dmitriev SV, Lee C, Kivshar YS. 2016 Nonlinear switching and solitons in PT-symmetric photonic systems. *Laser Photonics Rev.* **10**, 177–213. (doi:10.1002/lpor.201500227)
49. Xue LF, Gong ZR, Zhu HB, Wang ZH. 2017 PT symmetric phase transition and photonic transmission in an optical trimer system. *Opt. Express* **25**, 17 249–17 257. (doi:10.1364/OE.25.017249)
50. Leykam D, Flach S, Chong YD. 2017 Flat bands in lattices with non-Hermitian coupling. *Phys. Rev. B* **96**, 064305. (doi:10.1103/PhysRevB.96.064305)
51. Du L, Zhang Y, Fan C-H, Liu Y-M, Gao F, Wu J-H. 2018 Enhanced nonlinear characteristics with the assistance of a PT-symmetric trimer system. *Sci. Rep.* **8**, 2933. (doi:10.1038/s41598-018-21137-y)
52. Zhang Y-Y, Hu Z-X, Fu L, Luo H-G, Zhang X-F. 2021 Quantum tricriticality of chiral-coherent phase in quantum Rabi triangle. *Phys. Rev. Lett.* **127**, 063602. (doi:10.1103/PhysRevLett.127.063602)
53. Ashida Y, Gong Z, Ueda M. 2020 Non-Hermitian physics. *Adv. Phys.* **69**, 249–435. (doi:10.1080/00018732.2021.1876991)
54. Bergholtz EJ, Budich JC, Kunst FK. 2021 Exceptional topology of non-Hermitian systems. *Rev. Mod. Phys.* **93**, 015005. (doi:10.1103/RevModPhys.93.015005)
55. Wang Y-P, Wang W, Xue Z-Y, Yang W-L, Hu Y, Wu Y. 2015 Realizing and characterizing chiral photon flow in a circuit quantum electrodynamics necklace. *Sci. Rep.* **5**, 8352. (doi:10.1038/srep08352)
56. Lai C-Y, Di Ventra M, Scheibner M, Chien C-C. 2018 Tunable current circulation in triangular quantum-dot metastructures. *Europhys. Lett.* **123**, 47002. (doi:10.1209/0295-5075/123/47002)
57. Dugar P, Scheibner M, Chien C-C. 2020 Geometry-based circulation of local photonic transport in a triangular metastructure. *Phys. Rev. A* **102**, 023704. (doi:10.1103/PhysRevA.102.023704)
58. Bender CM. 2018 *PT symmetry: in quantum and classical physics*. Singapore: World Scientific.
59. Quijandria F, Naether U, Ozdemir SK, Nori F, Zueco D. 2018 PT-symmetric circuit QED. *Phys. Rev. A* **97**, 053846. (doi:10.1103/PhysRevA.97.053846)
60. Cao J, Silbey RJ. 2009 Optimization of exciton trapping in energy transfer processes. *J. Phys. Chem. A* **113**, 13 825–13 838. (doi:10.1021/jp9032589)
61. Jin L. 2018 Parity-time-symmetric coupled asymmetric dimers. *Phys. Rev. A* **97**, 012121. (doi:10.1103/PhysRevA.97.012121)
62. Jin L. 2018 Asymmetric lasing at spectral singularities. *Phys. Rev. A* **97**, 033840. (doi:10.1103/PhysRevA.97.033840)
63. Engelhardt G, Cao J. 2019 Tuning the Aharonov-Bohm effect with dephasing in nonequilibrium transport. *Phys. Rev. B* **99**, 075436. (doi:10.1103/PhysRevB.99.075436)
64. Downing CA, Zueco D, Martín-Moreno L. 2020 Chiral current circulation and $\mathcal{PT}$ symmetry in a trimer of oscillators. *ACS Photonics* **7**, 3401–3414. (doi:10.1021/acsphotonics.0c01208)

65. Downing CA, López Carreño JC, Fernández-Domínguez AI, del Valle E. 2020 Asymmetric coupling between two quantum emitters. *Phys. Rev. A* **102**, 013723. (doi:10.1103/PhysRevA.102.013723)
66. Gardiner C, Zoller P. 2014 *The quantum world of ultra-cold atoms and light, book I: foundations of quantum optics*. London, UK: Imperial College Press.
67. Barredo D, Ravets S, Labuhn H, Beguin L, Vernier A, Nogrette F, Lahaye T, Browaeys A. 2014 Demonstration of a strong Rydberg blockade in three-atom systems with anisotropic interactions. *Phys. Rev. Lett.* **112**, 183002. (doi:10.1103/PhysRevLett.112.183002)
68. Klauck F, Teuber L, Ornigotti M, Heinrich M, Scheel S, Szameit A. 2019 Observation of PT-symmetric quantum interference. *Nat. Photonics* **13**, 883–887. (doi:10.1038/s41566-019-0517-0)
69. Roushan P *et al.* 2017 Spectroscopic signatures of localization with interacting photons in superconducting qubits. *Science* **358**, 1175–1179. (doi:10.1126/science.aao1401)
70. Owens C, LaChapelle A, Saxberg B, Anderson BM, Ma R, Simon J, Schuste DI. 2018 Quarter-flux Hofstadter lattice in a qubit-compatible microwave cavity array. *Phys. Rev. A* **97**, 013818. (doi:10.1103/PhysRevA.97.013818)
71. Ma R, Saxberg B, Owens C, Leung N, Lu Y, Simon J, Schuster DI. 2019 A dissipatively stabilized Mott insulator of photons. *Nature* **566**, 51–57. (doi:10.1038/s41586-019-0897-9)
72. Dutt A, Lin Q, Yuan L, Minkov M, Xiao M, Fan S. 2020 A single photonic cavity with two independent physical synthetic dimensions. *Science* **6473**, 59–64. (doi:10.1126/science.aaz3071)
73. Zohar N, Chuntonov L, Haran G. 2014 The simplest plasmonic molecules: metal nanoparticle dimers and trimers. *J. Photochem. Photobiol. C* **21**, 26–39. (doi:10.1016/j.jphotochemrev.2014.10.002)
74. Lu G, Wang Y, Chou RY, Shen H, He Y, Cheng Y, Gong Q. 2015 Directional side scattering of light by a single plasmonic trimer. *Laser Photonics Rev.* **9**, 530–537. (doi:10.1002/lpor.201500089)
75. Barrow SJ, Collins SM, Rossouw D, Funston AM, Botton GA, Midgley PA, Mulvaney P. 2016 Electron energy loss spectroscopy investigation into symmetry in gold trimer and tetramer plasmonic nanoparticle structures. *ACS Nano* **10**, 8552–8563. (doi:10.1021/acsnano.6b03796)
76. Chen T-Y, Tyagi D, Chang Y-C, Huang C-B. 2020 A polarization-actuated plasmonic circulator. *Nano Lett.* **20**, 7543–7549. (doi:10.1021/acs.nanolett.0c03008)
77. Peropadre B, Zueco D, Wulschner F, Deppe F, Marx A, Gross R, Garcia-Ripoll JJ. 2013 Tunable coupling engineering between superconducting resonators: from sidebands to effective gauge fields. *Phys. Rev. B* **87**, 134504. (doi:10.1103/PhysRevB.87.134504)
78. Baust A *et al.* 2015 Tunable and switchable coupling between two superconducting resonators. *Phys. Rev. B* **91**, 014515. (doi:10.1103/PhysRevB.91.014515)
79. Asensio-Perea R, Parra-Rodriguez A, Kirchmair G, Solano E, Rico E. 2021 Chiral states and nonreciprocal phases in a Josephson junction ring. *Phys. Rev. B* **103**, 224525. (doi:10.1103/PhysRevB.103.224525)
80. Kiefer P, Hakelberg F, Wittemer M, Bermudez A, Porras D, Warring U, Schaetz T. 2019 Floquet-engineered vibrational dynamics in a two-dimensional array of trapped ions. *Phys. Rev. Lett.* **123**, 213605. (doi:10.1103/PhysRevLett.123.213605)
81. Barredo D, Labuhn H, Ravets S, Lahaye T, Browaeys A, Adams CS. 2015 Coherent excitation transfer in a spin chain of three Rydberg atoms. *Phys. Rev. Lett.* **114**, 113002. (doi:10.1103/PhysRevLett.114.113002)
82. Lienhard V *et al.* 2020 Realization of a density-dependent Peierls phase in a synthetic, spin-orbit coupled Rydberg system. *Phys. Rev. X* **10**, 021031. (doi:10.1103/PhysRevX.10.021031)
83. Aidelsburger M, Atala M, Nascimbene S, Trotzky S, Chen Y-A, Bloch I. 2011 Experimental realization of strong effective magnetic fields in an optical lattice. *Phys. Rev. Lett.* **107**, 255301. (doi:10.1103/PhysRevLett.107.255301)
84. Aidelsburger M, Atala M, Lohse M, Barreiro JT, Paredes B, Bloch I. 2013 Realization of the Hofstadter Hamiltonian with ultracold atoms in optical lattices. *Phys. Rev. Lett.* **111**, 185301. (doi:10.1103/PhysRevLett.111.185301)
85. Atala M, Aidelsburger M, Lohse M, Barreiro JT, Paredes B, Bloch I. 2014 Observation of chiral currents with ultracold atoms in bosonic ladders. *Nat. Phys.* **10**, 588–593. (doi:10.1038/nphys2998)
86. Gou W, Chen T, Xie D, Xiao T, Deng T-S, Gadway B, Yi W, Yan B. 2020 Tunable nonreciprocal quantum transport through a dissipative Aharonov-Bohm ring in ultracold atoms. *Phys. Rev. Lett.* **124**, 070402. (doi:10.1103/PhysRevLett.124.070402)